

ConvNets for counting: Object detection of transient phenomena in steelpan drums

Scott H. Hawley and Andrew C. Morrison

Citation: *The Journal of the Acoustical Society of America* **150**, 2434 (2021); doi: 10.1121/10.0006110

View online: <https://doi.org/10.1121/10.0006110>

View Table of Contents: <https://asa.scitation.org/toc/jas/150/4>

Published by the [Acoustical Society of America](#)

ARTICLES YOU MAY BE INTERESTED IN

[Toward a physical model of the clavichord](#)

The Journal of the Acoustical Society of America **150**, 2350 (2021); <https://doi.org/10.1121/10.0006438>

[Three-dimensional spiral motion of microparticles by a binary-phase logarithmic-spiral zone plate](#)

The Journal of the Acoustical Society of America **150**, 2401 (2021); <https://doi.org/10.1121/10.0006417>

[Resolvent-based modeling of turbulent jet noise](#)

The Journal of the Acoustical Society of America **150**, 2421 (2021); <https://doi.org/10.1121/10.0006453>

[Automated partial differential equation identification](#)

The Journal of the Acoustical Society of America **150**, 2364 (2021); <https://doi.org/10.1121/10.0006444>

[In situ characterization of laser-generated melt pools using synchronized ultrasound and high-speed X-ray imaging](#)

The Journal of the Acoustical Society of America **150**, 2409 (2021); <https://doi.org/10.1121/10.0006386>

[Angle-dependent sound absorption estimation using a compact microphone array](#)

The Journal of the Acoustical Society of America **150**, 2388 (2021); <https://doi.org/10.1121/10.0006566>



**Advance your science and career
as a member of the
ACOUSTICAL SOCIETY OF AMERICA**

[LEARN MORE](#)



ConvNets for counting: Object detection of transient phenomena in steelpan drums^{a)}

Scott H. Hawley^{1,b)} and Andrew C. Morrison^{2,c)}

¹Department of Chemistry & Physics, Belmont University, Nashville, Tennessee 37212, USA

²Natural Science Department, Joliet Junior College, Joliet, Illinois 60431, USA

ABSTRACT:

We train an object detector built from convolutional neural networks to count interference fringes in elliptical antinode regions in frames of high-speed video recordings of transient oscillations in Caribbean steelpan drums, illuminated by electronic speckle pattern interferometry (ESPI). The annotations provided by our model aim to contribute to the understanding of time-dependent behavior in such drums by tracking the development of sympathetic vibration modes. The system is trained on a dataset of crowdsourced human-annotated images obtained from the Zooniverse Steelpan Vibrations Project. Due to the small number of human-annotated images and the ambiguity of the annotation task, we also evaluate the model on a large corpus of synthetic images whereby the properties have been matched to the real images by style transfer using a Generative Adversarial Network. Applying the model to thousands of unlabeled video frames, we measure oscillations consistent with audio recordings of these drum strikes. One unanticipated result is that sympathetic oscillations of higher-octave notes significantly precede the rise in sound intensity of the corresponding second harmonic tones; the mechanism responsible for this remains unidentified. This paper primarily concerns the development of the predictive model; further exploration of the steelpan images and deeper physical insights await its further application. © 2021 Acoustical Society of America.

<https://doi.org/10.1121/10.0006110>

(Received 1 February 2021; revised 16 August 2021; accepted 18 August 2021; published online 6 October 2021)

[Editor: Bozena Kostek]

Pages: 2434–2445

I. INTRODUCTION

Electronic Speckle Pattern Interferometry (ESPI) has proven to be an effective technique for musical acoustics research. ESPI provides a means for the measurement and visualization of vibrating plates and membranes making up musical instruments such as violins, guitars, drums, and others.^{1,2} ESPI offers the capability of making amplitude measurements for small vibrations; time-averaged ESPI produces images with light and dark fringes, which are lines of constant surface deformation proportional to the wavelength of the laser light. These images are similar to Chladni patterns in that they reveal the mode shapes of vibrating surfaces (although typically, Chladni patterns are used to reveal standing wave patterns, whereas the images in the present paper are of transient phenomena). While lacking the full spatial resolution of traditional film-based laser holography images,³ the relatively low cost and ease of setup make ESPI a popular choice for researchers and educators.⁴

High-speed video of ESPI images has been used in the case of Caribbean steelpan drums.⁵ The steelpan drum is a membranophone that originated in Trinidad and Tobago. Instrument-makers repurposed steel oil drums,⁶ stretching the steel into a concave surface and dividing it into a set of

flattened, tuned subdomains often referred to simply as “notes.” It is played using straight sticks tipped with rubber. When a particular note is struck, waves emanate from the point of impact. At the boundary for the note, some of the wave energy is reflected and sets up standing waves,⁷ while the remainder propagates throughout the full steelpan domain and triggers sympathetic vibrations among the other notes. An accurate characterization of the sympathetic vibration time evolution has yet to be realized.^{8,9} A fundamental question is how much of the sound of the drum is due to nontrivial time-dependent behavior of the drum notes (as opposed to steady-state resonant modes).

To better understand the full dynamics at work in the steelpan, high-speed ESPI images merit closer, quantitative measurements, and yet the enormous quantity of frames recorded poses a burden on researchers to properly annotate and catalog what is seen in the images. Thus, the “Steelpan Vibrations Project” (SVP)¹⁰ was formed in partnership with the Zooniverse.org¹¹ platform for crowdsourced data analysis. Zooniverse arose in the context of large-scale sky surveys of galaxies, relying on human volunteers from around the world to use a World Wide Web interface to annotate the images and classify the galaxies seen in the images.¹² The specific nature of the annotation used in the SVP will be described in Sec. II A. As the SVP progressed, it became apparent that an insufficient number of volunteers were contributing to the project, such that progress in annotating the large dataset of images was slow. In addition,

^{a)}This paper is part of a special issue on Machine Learning in Acoustics.

^{b)}Electronic mail: scott.hawley@belmont.edu, ORCID: 0000-0002-5743-6441.

^{c)}ORCID: 0000-0003-2676-4087.

because of the variation in human annotators' work, having multiple volunteers' annotations of the same image was deemed necessary,¹³ further slowing the progress of using these annotations to understand the dynamics of the steelpan. Thus, the use of automated annotation methods merited exploration.

While traditional methods of ellipse detection, such as the Elliptical Hough Transform¹⁴ can be effective for smooth, well-defined ellipse features, the noisy and highly variable nature of the ellipse regions in SVP images, combined with the additional task of counting the rings per antinode, make the Elliptical Hough Transform a poor fit for this task. There are adaptions to account for incomplete shapes and noise;^{15,16} however, the presence of labels via the SVP made us interested in a machine-learning approach. Thus, we sought to adapt methods of neural network-object detection models to our unique use case.

The success of machine-learning systems at extending the image-annotation efforts of humans has been demonstrated in a variety of domains—notably, image-classification challenges involving the recognition of handwritten numerical digits¹⁷ and images of various animals and vehicles.^{18,19} The task of localizing and classifying portions of images is known as “object detection;”²⁰ typical uses include surveillance systems and satellite imagery analysis²¹ as well as astronomy applications²² such as galaxy classification.²³

Multiple algorithms exist for object detection, and among the most popular and successful in recent years^{24–26} are those that rely on convolutional neural networks (CNN) that reduce each image into a (large) set of learned features. These features are then fed into a fully-connected layer to predict locations of objects and their classifications. The scheme used for SPNet is inspired by that of YOLOv2,²⁷ but uses one of a variety of “stock” CNN base models, along with a few important modifications specific to the domain of ESPI imagery of steelpan drums, and the annotation task of the SVP, as follows: Most object detectors operate on color images of everyday objects, animals, and people found in datasets such as ImageNet,²⁸ whereas the SVP task required the resolution of constantly changing patterns in grainy, grayscale images. Most object detectors provide classifications of their objects, whereas the SVP task required regression to “count” interference fringes. While CNNs are known to perform well at detecting and classifying textures^{29,30} or for counting numbers of objects or people,³¹ their use to “count” rings (or, phrased more carefully, to discover correlations between image patterns and ring counts) which may have similar “texture” but different spatial extents, was not an application that we observed to have received widespread attention. Most object detectors make location predictions for rectangular regions of images, whereas the SVP required tracking antinodes within elliptical regions. When we began work in 2017, elliptical object detectors were not in widespread use; however, while preparing this paper, a classifier for wood knots was published³² which uses a different scheme from what we present here.

The paper is organized as follows: Sec. II presents details of the SPNet algorithm and training. Section III presents some performance metrics, Section IV presents preliminary physics results, and Sec V provides a discussion of these results. A separate paper discussing these and further physics results is in preparation.

For the purpose of reproducibility, the SPNet computer code is available at <https://github.com/drscothawley/spnet>, and two of the datasets used have been released on Zenodo.³³

II. SPNET DESIGN

A. The Steelpan Vibrations Project (SVP)

Volunteers recruited for the SVP are presented with randomly selected frames from high-speed videos, such as the grayscale image shown in Fig. 1(a), and are tasked with using a web interface to place elliptical boundaries around the antinode regions (as shown in green), along with counting the number of interference fringes or “rings” for each antinode. Multiple videos for different steelpan-strokes are available, which show different regions of the (same) steelpan being excited.

The frames that are included in the SVP are taken from an ESPI optical arrangement and were captured by a high-speed camera and processed by image subtraction of a reference frame from individual video frames after the drum has been struck. The drum was struck on the back side of the note such that the front side of the note would be unobstructed to the camera's view. The drum was struck with a metal ball driver held by hand at amplitudes well below the typical playing conditions. The vibration amplitudes must be small to be able to be seen clearly in the ESPI frames.

For the SVP classification task, organizers required that at least 15 people supply annotations for a given video frame (image) before it could be analysed for clustering¹³ and then for each antinode in a frame, at least five annotations would be needed. For example, for an image with three

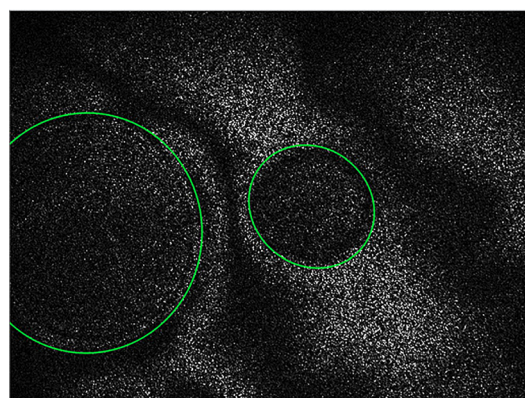


FIG. 1. (Color online) Illustration of Steelpan Vibrations Project (Ref. 10) (SVP) task: Ellipses “drawn” (in green) by human annotators around antinodes in an ESPI steelpan video frame via the Zooniverse crowd-sourcing data annotation interface. Not shown: Annotations also include users' counts of the number of interference fringes or rings for each antinode region.

antinodes, ideally there would be 45 annotations, which were grouped via cluster in X and Y directions. If a volunteer's suggestion was too far from the average (e.g., their mouse slipped) then it was not considered. Then, averages were performed over the ellipse parameters and number of fringes; these averages were written to a file, which comprised the "raw" or "ground truth" data for training the SPNet model. As indicated in Fig. 2, from frame-to-frame, some antinode regions will appear or disappear. Beyond variability among volunteers, it can be very much a "human judgement call" as to whether a given ring-shape should be marked as an antinode or not; volunteers were exposed to one frame at a time rather than viewing video. Even with the benefit of viewing multiple frames, to the authors of this paper (who may be considered to provide an "above-average" level of consistency as annotators), it is not always clear—especially immediately after a strike—which shapes to mark as antinodes. Furthermore, often the struck note would exhibit a "twin antinode" structure resulting from its excited 2nd harmonic, in which case annotators may have drawn an ellipse around the whole note or drawn two ellipses around the two (alternating) sections of the note. This is perhaps at variance with the experience of many machine-learning enthusiasts who are accustomed to working with very clean datasets and/or well-defined tasks. To better clarify the difficulty of performing the task with consistency, we invite readers to visit the SVP website¹⁰ and try annotating several images themselves. Continuing our example from above, if 11 of the 15 people missed one of the three antinodes, then it would be rejected and not included in the dataset at all for that frame.

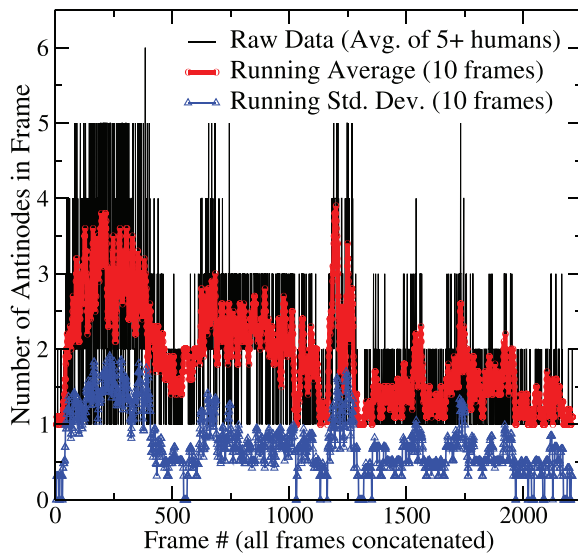


FIG. 2. (Color online) Graphical representation of one aspect of the variability in the aggregated human annotations comprising the SVP dataset. While physically, antinodes typically persist over 50 to hundreds of frames, the fine structure of the raw data in this graph shows that the presence of some antinodes may or may not have been annotated consistently frame-by-frame (even in the aggregated data). This is the dataset used to train and score the SPNet model. This does not display (the further) variability in ring counts, only whether an antinode is marked.

Regarding the variability in volunteers' ring counts: When we compute the standard deviations of volunteers' ring counts of each antinode and average over all antinodes, we find a value of 1.7. This is considerably wider than the ± 0.5 used for scoring the SPNet model's accuracy, below. For a standard deviation of 1.7, the area under a normal probability distribution within ± 0.5 of the mean is approximately 0.23, which implies a typical volunteer's ring-count accuracy metric for comparison with SPNet would be 23%.

The task of SPNet is to match (average) human performance from the SVP for the frames available, as well as to "fill in" the missing annotations for frames in-between those already annotated by volunteers. The specificity of this goal will affect the design of the training, discussed in Sec. II D—the design goal of "filling in" missing frames means that the trained SPNet model is not intended to serve as a generic "deployable" inference model for general ESPI images that differ qualitatively from those in the SVP dataset. Questions regarding the ability of the SPNet model to generalize to other ESPI images, such as those of guitars are addressed in Sec. V.

B. Model architecture

The overall strategy of SPNet is inspired by YOLOv2,²⁷ but the model differs in that we use one of several pre-defined "stock" multi-layered CNN architectures for the main convolutional network, such as MobileNet,³⁵ InceptionResnetV2,³⁶ or Xception.³⁴ The ability to easily swap in various predefined CNN base models is made possible *via* the Keras neural network framework.³⁷ These models can be initialized using random weights or weights pre-trained on Imagenet.³⁸ Our experience indicates that the Xception³⁴ provides a good base model yielding high accuracy, stable training, and reasonable execution time. (MobileNet, although faster, was not as accurate, whereas InceptionResNetV2 proved both slower and more difficult to train consistently.) These base models typically expect square-shaped image inputs with three color channels, and large input images can result in networks with so many tunable parameters (weights) that their memory requirements exceed the capacities of single computer workstations. In order to supply input images compatible with available pre-trained base model architectures, while keeping memory requirements manageable, we first resize our 512×384 grayscale input images to a square size of 331×331 . Even this proves to be unnecessarily and prohibitively memory-intensive, so we shrink this by a factor of two using "average pooling," and then "tile" (i.e., repeat or broadcast) the grayscale channel to form three identical "color" channels—this is the lower path shown in Fig. 3. Doing this alone, however, could result in some loss in fine detail, so we combine the lower path with the result of the "upper path," consisting of multiple 3×3 convolutions yielding three filter channels, in concert with a pooling operation for size reduction. Adding these two paths forms a "residual block"¹⁹ for which the lower (pool-tile) path is a skip connection. The skip connection allows the model to train faster than without it by

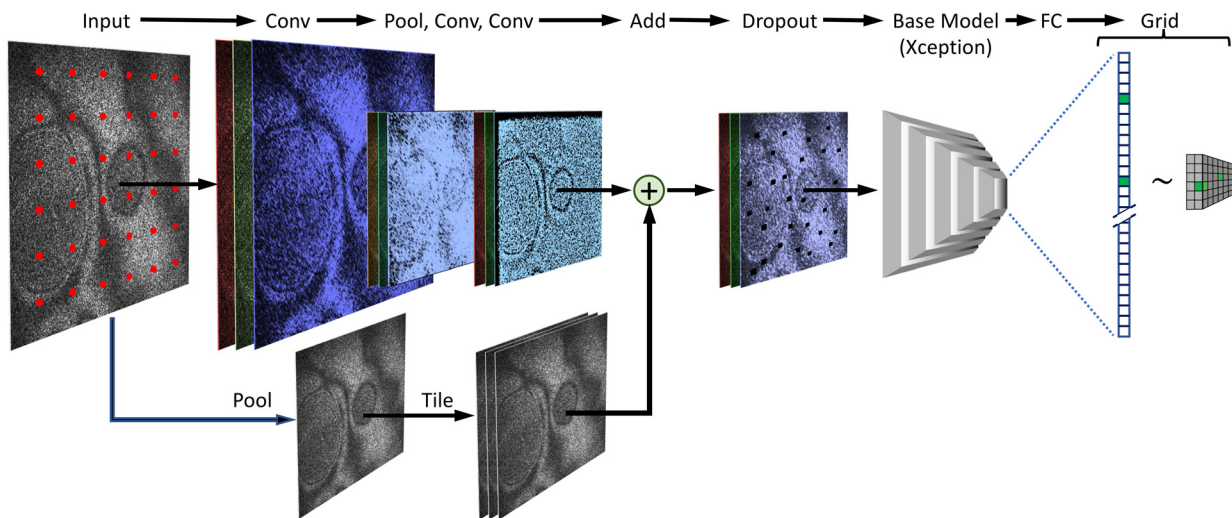


FIG. 3. (Color online) Diagram of the SPNet architecture. The grayscale input image is resized via average pooling and two additional (“color”) channels are added via 3×3 convolutions before feeding into a “stock” base model chosen from available Keras models (as described in the text, we prefer Xception (Ref. 34) which is then fully connected to a flattened layer which holds the values of a $6 \times 6 \times 2$ grid of predictors for the 8 variables in Table I. $(6 \times 6 \times 2 \times 8 = 576)$ values in the model output.) The operations to the left of the base model can be regarded as a “residual block” designed to shrink the image to lower memory costs while still retaining some finer details of the larger input image. Also, shown as an array of red dots on the input image are the centroids of regions covered by the predictors, which predict antinode centroid coordinates in terms of offsets from these locations. Not shown: Leaky ReLU activations and batch normalization between layers. (Note: the images shown for intermediate layers are “artwork,” not actual layer activations.)

smoothing the hypersurface of the loss function,³⁹ and the upper (conv-pool-conv-conv) path allows the model to better resolve fine features from the larger (331×331) image before reducing it in size to feed into the base model. The pre-processing layers (before the base model) include Leaky ReLU activations and batch normalization. We also add a small amount (0.1) of dropout⁴⁰ before the base model to help avoid overfitting.

The output of the base model is fully connected to a “flattened” layer whose elements are taken to represent a “grid” of outputs we refer to as “predictors” which predict attributes of relevant antinodes for each subdomain of the image covered by the predictor. Each predictor predicts 8 values shown in Table I: (p, x, y, a, b, s, c, r) , where these values are defined relative to the subdomain associated with each predictor, i.e., within each “grid cell,” according to Table I. The “existence” variable $p \in [0..1]$ measures the distinction between the background and an object. The values of x , y , a and b are normalized relative to the size of the image, and x and y are offsets from the center of each respective grid point. Instead of the ellipse rotation angle θ , we use the two variables $c \equiv \cos(2\theta)$ and $s \equiv \sin(2\theta)$ which have the dual advantages of avoiding any coordinate discontinuity at $\theta=0$ as well as ensuring uniqueness given the 180° rotational symmetry of the ellipses.⁴¹ These variables are later used in training by optimizing the loss function, which appears in Sec. II D 1 as Eq. (1).

C. Datasets

Table II summarizes the datasets used in this study. Early in this project, there were insufficient numbers of (aggregated) volunteer-annotated images, so in order to

develop and test the model, we procedurally generated a large (50 000 image) corpus of random “fake” images that combine these salient features: groups of elliptical rings of varying sizes, orientations, eccentricities, on a background of wavy patterns, with noise. (We prefer the word “fake” over the more formal “synthetic” to avoid any confusion—these images are akin to “artwork” and have no physical basis). Shown in the upper pane of Fig. 4 is an example of the fake data comprising the FakeLarge dataset, along with superimposed “exact” annotations (upper values, light yellow) and SPNet predictions (lower values, dark purple.) The fake images in FakeLarge are quite different from the Real data in that the former have sharp edges and lack the variations in brightness, contrast, blurriness, and lost pixels observed in the latter.

Additional datasets were created after it was observed that the model’s performance when training on the FakeLarge dataset (e.g., Figure 5) was much better than when the Real dataset was used. Questions about the cause of this discrepancy in performance between datasets included:

1. Was it because there was more data in FakeLarge than Real?

TABLE I. Definitions of predicted variables.

p :	the probability of an antinode’s existence within the grid cell, $p \in [0..1]$
x, y :	coordinates of the offset of the antinode’s centroid relative to the grid cell’s center on the image
a, b :	the ellipse’s semimajor and semiminor axes ($a >= b$)
c, s :	$c \equiv \cos(2\theta)$ and $s \equiv \sin(2\theta)$, where θ is the ellipse orientation angle
r :	the number of rings (i.e., interference fringes)

TABLE II. List of datasets, each divided into Train/Validation/Test subsets as 80%/10%/10% splits. Due to RAM limits, all Train subsets contain 40 000 images, where smaller initial sets have training subsets (~960 images) augmented by a factor of 41 to produce 40 000 images (see “Data augmentation”). “Fake” denotes synthetic images, used as a consistent baseline given the inconsistency of the human-annotated “real” images. Bold for the rows indicates that these are the most similar for judging the effects of variability in the human labels in Real (whereas those in CGSmall are “exact”). Datasets FakeLarge and CGLarge are available from Zenodo;³³ whereas release of the Real Read dataset is delayed pending a future paper.

Label	Description
FakeLarge	Fake, 50 000 images
Real	Real data, \approx 1200 images
FakeSmall	1200-image subset of FakeLarge
CGLarge	CycleGAN-processed FakeLarge
CGSmall	1200-image subset of CGLarge

2. Was it because antinode boundaries and rings were much clearer in FakeLarge images than in Real?
3. Was it because the annotations in FakeLarge were exact, whereas the annotations in Real were highly variable, i.e., similar-looking images in Real often had very different annotations (thus “confusing” the ML system as it trained), and/or causing it to rate low scores on evaluations metrics like “Accuracy”?

To explore the first question, we created the FakeSmall dataset and found that dataset size was not a major factor. To answer question 2, we matched the visual properties of the real data (i.e., the statistics of the pixels in the images) while still retaining “exact” annotations against which to evaluate the model, by training a CycleGAN⁴² model to do neural style transfer, applying the style of real images to those in FakeLarge. These results were termed CGLarge, one example of which is shown in the lower pane of Fig. 4. We also created a corresponding smaller set termed CGSmall. The implications of this being that the difference in performance between CGSmall and Real would provide a measure of the degradation in model performance due to the

inconsistency in the volunteers’ aggregated annotations in Real. As you will see below in Fig. 5 and Table III, the difference is significant.

1. Data preparation

We obtained a set of aggregated data from multiple volunteers’ annotation attempts;¹³ although the users’ ring counts were entered as integers, the aggregation process produces decimal ring counts. The main data preparation work for SPNet lies in taking the aggregated SVP data and setting up the correct vector of target values Y for all grid cells, for all images, in a way that would be unambiguous and thereby “easiest” for the system to learn.

First, we initialize all predictors to indicate no existence, i.e., $p=0$, and for all other variables to be set in the middle of their respective (normalized) ranges. Then, for each set of annotations (for each image), also called “metadata,” we sort the antinodes by their centroid locations, first vertically and then horizontally, then compute to which grid cell each antinode “belongs”. For the first of the two predictors in that cell, we set $e=1$, compute x and y as the difference between the antinode’s centroid coordinates and the center of the grid cell, divided by the width of the grid cell to keep the values normalized on $-0.5\dots0.5$. It is possible that the Zooniverse interface allowed for $a < b$ and/or for a given rotation angle θ that may not be bounded within a 180° range; so, for definiteness, we swap a and b for any data in order to enforce $a > b$, subtracting 90° in the process. After this, we compute $c = \cos 2\theta$ and $s = \sin 2\theta$ to enforce the twofold rotational symmetry of the ellipses as well as avoid any ambiguities with positive or negative angles, or coordinate singularities at $\theta=0$. This process is repeated, with the second predictor in a cell being used if there has already been an antinode found in a given grid cell. (For more intricate patterns of antinodes, more predictors per cell, and/or a more finely grained grid of predictors could be used. The choice of $6 \times 6 \times 2$ was found to be adequate for the SVP data.) Having set up all the target or



FIG. 4. (Color online) Sample fake images, showing ground-truth bounding ellipses and ring counts (upper values, light yellow) and those predicted by the network (lower values, dark purple). Top: original style of fake image, from FakeLarge dataset. Bottom: same fake image with “real” style transferred via CycleGAN (Ref. 42), from CGLarge dataset.

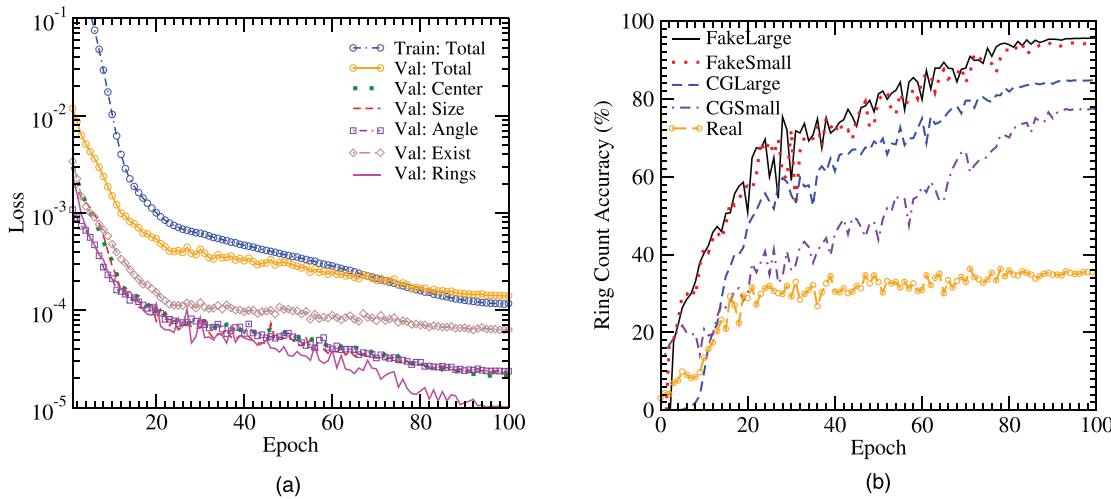


FIG. 5. (Color online) Training progress. Top: various components of the loss function for dataset FakeLarge. (A similar graph for Real would show Validation loss values leveling off after approximately 20 epochs, which is where the Training loss crosses the Validation loss.) Bottom: Classification-like accuracy scores for ring counts for validation subsets of all datasets. Despite FakeSmall, CGSmall, and Real all having similar numbers of training images (ca. 1200, when are then augmented as per Sec. II C2), FakeLarge and CGSmall have much higher accuracy scores than Real. The fact that the accuracy for Real does not improve beyond Epoch 20 indicates the variability of the human-supplied data annotations.

“true” output data Y for the grid of predictors to be trained against, it is possible to begin computing a loss function. First, however, it is necessary to augment the input data to improve the generalization performance of the model.

2. Data augmentation

Augmenting the Training set is a common regularization technique used during the training of machine-learning systems to increase the variance of a dataset and thus make a trained model more robust, i.e., to improve its generalization performance when operating on new images. It is crucial in relatively small datasets, such as the $\simeq 1200$ images obtained from the SVP. We perform augmentations at two different stages.

The first stage consists of preprocessing augmentations that (randomly) change both the images and annotations together—rotations ($\pm 10^\circ$), translations (± 40 pixels), and reflections—as well as some image processing, such as noise or blurring.

The second set of augmentations is performed “on the fly” at the start of each training epoch, on all input images from the first stage, and consists of random changes to the images only without altering the annotations,⁴³ such as blurring, adding noise, and “cutout”⁴⁴ (i.e., excising multiple rectangular subdomains), or changes to brightness or contrast. The on-the-fly augmentations applied once per epoch for 100 epochs to $\approx 40\,000$ training images from each dataset (after the first set of augmentations) mean that during training, the model is trained on approximately 4×10^6 different images for each dataset.

D. Training procedure

1. Loss function

Training is structured as a supervised regression problem using mean squared error (MSE) loss for all variables,

subject to a few caveats as follows. For compactness, we use the symbol Δ_u^2 to denote the squared error for a variable $u \in \{p, x, y, a, b, c, s, r\}$, so e.g., $\Delta_x^2 \equiv (\hat{x} - x)^2$, with predicted values denoted by “hats.” In this notation, we define the loss function L_j for each grid-based predictor j , weighted by the ground truth existence p ($= 0$ or 1) of an antinode in each region, with constant scaling factors λ_u (tuned by experience so that the terms in the sum are all comparable in magnitude) to be given by:

$$L_j = -\lambda_p \Delta_p^2 + p \left[\lambda_{\text{center}} (\Delta_x^2 + \Delta_y^2) + \lambda_{\text{size}} (\Delta_a^2 + \Delta_b^2) + \lambda_{\text{angle}} (a - b)^2 (\Delta_c^2 + \Delta_s^2) + \lambda_r \Delta_r^2 \right]. \quad (1)$$

The total loss $L = (1/N) \sum_{j=1}^N L_j$ is then the mean over all predictors j , with $N = 6 \times 6 \times 2 = 72$ being the total number of predictors in the output grid. The term in brackets in Eq. (1) is scaled by the ground truth object existence probability p ($= 0$ or 1), because without existence, all other quantities have no ground truth values. The use of the squared difference $(a - b)^2$ to scale the contribution due to the angle reflects the intention that, the more circular an ellipse is, the less its angular orientation should matter.

[Replacing the first term in the loss Eq. (1) with a cross-entropy term, i.e., $-\lambda_p [p \log(\hat{p}) + (1 - p) \log(1 - \hat{p})]$, was found to confer no appreciable improvement to the results.]

We also add an L2 regularization or “weight decay”^{45,46} with strength 1E-4 to all layers in the Keras model;⁴⁷ we find this regularization to be important for avoiding overfitting.

2. Model Initialization

Although it is possible to initialize the base model supplied by Keras using weights pre-trained on ImageNet, the different nature of our images (grainy grayscale ESPI rather

than color images of common objects, animals, vehicles, etc.) and our intended output type (regression rather classification) made these pre-trained weights of little utility, and no better than random initialization. Thus, we train all model layers from random initial weights.

III. MODEL PERFORMANCE AND EVALUATION

The purpose of the SPNet model is to help with SVP annotations with the goal of obtaining physical insight into the motion of drums, not to lay claim to “state-of-the-art” status in object detection nor win a Kaggle competition, nor to provide a general utility for generic interference measurements, nor to offer real-time computational efficiency. Nevertheless, it is important for a method such as ours to yield reliable results in a timely manner, and for this reason, we provide measurements of training progress and accuracy scores. Sample graphs for training progress in terms of loss (component) values and accuracies are shown in Fig. 5. We typically trained for 100 epochs using an Adam optimizer and “1-cycle” learning rate schedule^{48,49} with cosine annealing,⁵⁰ using a maximum learning rate of $4e-5$. These runs would take 8 h on a machine fitted with an RTX 2080Ti GPU (Santa Clara, CA).

Object detection models are usually evaluated in terms of classification and localization. Given that our task is one of regression rather than classification, many object detection metrics do not apply directly. However, we emulate the task of an individual human in the SVP (who provided integer values for ring counts up to 11—in which each integer could be regarded as a class), by considering whether the model’s prediction is within ± 0.5 of the ground truth value.⁵¹ Using this, we produce a “ring count accuracy” metric, as follows: We take the number of matching ring counts between ground truth and predictions and divide it by the total number of ground truth objects (antinodes) in the Validation dataset. For example, 168 matching ring counts out of 482 ground truth objects would yield an accuracy score of 35%. For comparison, we noted in Sec. II A that the standard deviation of individual human volunteers contributing to the aggregated ground truth data imply that a typical volunteer subjected to a similar metric would score a ring count accuracy of 23%.

For an additional metric that applies only to antinode object detection and not ring counts, we compare the aggregated responses by human users in the SVP to the model predictions, according to the following metrics: precision (i.e., number of true object detections divided by the total number of objects predicted by the model), recall (i.e., true object detections divided by the total number of objects in the aggregated human data), and intersection-over-union score (IoU), i.e., the fraction of area overlap between predicted ellipses and their ground truth counterparts. These can be combined into a single metric known, as the mean average precision (mAP),⁵² which has been averaged over a set of multiple detection thresholds (i.e., this mAP is comparable to the “COCO mAP”⁵³ with the single category of

foreground-versus-background detection). These scores are listed in Table III. As a baseline comparison, the Real dataset was converted to rectangular bounding boxes and processed using the object-detection package IceVision,⁵⁴ yielding similar mAP scores of 0.62 and 0.63 using IceVision’s Resnet50 and YoloV5 models, respectively.⁵⁵

We attribute the low accuracy on the Real dataset to the inconsistency of human annotations, rather than the size of the training corpus, because scores for CGSmall (which has a similar number of images with similar features but consistent annotations) are significantly higher. The difference between results for the two datasets becomes even more striking when one considers that the Real data has less variability in images compared to CGSmall, because for the former, the antinodes in a given video clip stay in only a finite number of places, and the nature of “filling in” missing annotations between frames implies that images randomly allocated among the Training and Validation sets will contain many near-duplicates—in other words, for the Real data, one might expect artificially high scores due to “cheating.” In contrast, in CGSmall, the antinodes are distributed randomly everywhere, thus making it more difficult for the model to memorize their existence, locations, and sizes. Furthermore, increasing the Training set when scoring against the Validation set for the Real dataset, for example, by combining the Training portions of CGLarge and Real, confers no noticeable change in the evaluation scores, because again, the evaluation data for Real is highly variable. Even after “data cleaning” by the authors’ manually editing the annotations for all 1200 images in Real, there was no uniform consistency, as the annotation involves many “judgment calls” of whether an antinode is present, and if so, how many rings should be counted. Future annotation efforts may benefit from using more than one frame at a time, such as viewing the stack of frames as a 3D volume and annotating via the kinds of software used in medical imaging and segmentation. Greater refinement of the model architecture and hyperparameter tuning would likely produce increases in the already-high evaluation scores on the synthetic datasets (FakeLarge through CGSmall); however, the limiting factor of the variability in the Real dataset’s annotations implies that continued revision of the model would have little effect on the metrics for the Real data,

TABLE III. Scores for accuracy and mean average precision (mAP) for models trained for 100 epochs from the same random initial weights. “Accuracy” is defined as number of matching ring counts (within ± 0.5) divided by total ground truth objects, whereas mAP indicates antinode detection rate⁵² over a range of detection thresholds and is independent of ring count.

Dataset	Accuracy	mAP
FakeLarge	0.95	0.97
Real	0.35	0.67
FakeSmall	0.94	0.95
CGLarge	0.89	0.89
CGSmall	0.77	0.78

from which we wish to extract measurements of physical phenomena. We anticipate that through additional cleaning of the dataset (i.e., improving the consistency of the annotations), that the accuracy score will rise accordingly.

Given the difficulty in scoring the model's accuracy on real data, a concern arises about whether attempts to extract physics from the model's annotations are sufficiently warranted. While this concern merits further study, two additional consistency checks give us reasons for optimism. First, curve fits of the model's time-series predictions of ring counts for octave notes yield close agreement with the known frequencies of those notes, such as a fit of 660 Hz obtained for the ring counts of the octave note when E₄ (= 330 Hz) is struck, and a fit of 596 Hz for the octave note when D₄ (= 294 Hz) is struck as shown in Fig. 6. The curve fit used was an absolute-value of cosine, which is chosen as the ring count, cannot be a negative value. The curve fit successfully matched the frequencies of the octave note for five of the seven recorded strikes for which the SPNet model was used to generate predictions of ring counts. The two cases where the model was unable to make predictions leading to a reliable curve fit are due to the amplitude of the drum strike being not sufficiently large enough to generate motion in the octave note that could be detected by the ESPI system. A graph showing a detail of one such sinusoidal fit is shown in Fig. 6.

Second, our inspection of the predictions of the model when applied to un-annotated video frames (such as in the sample movie at <https://youtu.be/-rJLwcbQ7Kk>) confirms that SPNet's predictions of both antinode boundaries and ring counts are consistent with our own estimations. Given these reasons for cautious optimism, Sec. IV, we begin to explore what physics may be ascertained when one is willing to take the many thousands of new frame-annotations

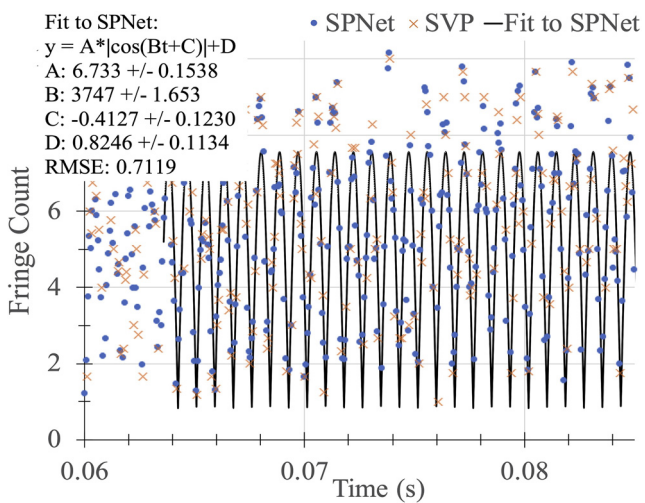


FIG. 6. (Color online) A segment of the SPNet amplitude predictions (circles) for the region of the steelpan corresponding to the D₅ note is fit with an $|\cos \omega t|$ function. The fitting parameter B is equivalent to ω . In this case $f = \frac{\omega}{2\pi} = 596$ Hz, which is close to the frequency of the D₅ note. (Note that this is a constant-amplitude fit in order to find the frequency.) Human annotations (SVP, x's) are included for comparison.

provided by the model at face value, with the caveat that these are preliminary results.

IV. PRELIMINARY PHYSICS RESULTS

Figure 7 shows drum oscillation amplitude as a function of time, comparing ring counts obtained from SPNet with audio recordings using a microphone placed 1m from the center of the drum. Each recording of a drum strike was made using an ACO Pacific (Belmont, CA) model 7012, $\frac{1}{2}$ condenser microphone controlled by a custom LabView (Austin, TX) program triggered to coincide with the high-speed ESPI recording. Audio recordings were made at a sample rate of 44 100 Hz, and analysis of the recordings was done with the SNDAN package.⁵⁶ The large fundamental note, such as that shown in the left of the field of view (as shown in Fig. 1) is struck, and the SPNet analysis tracks the rings in a note to the right, corresponding to the second harmonic. (This was confirmed by measuring the frequency of the oscillations in the ring counts.)

Figure 8 explores the relationship between the number of rings and the size (area) of the antinodes. For large ring counts, which indicate large deformation (or velocity) of the surface, one would expect the area of the antinode to be the same as that of the note itself. Small areas and small ring counts could result from small notes or could result from large note areas in which the note is barely moving. In the latter case, one would only see the shape of the largest portion of the note that "peeks up" above the threshold set by the laser interference. It is not obvious, then, what the relationship between area and ring count should be, and thus, we provide Fig. 8 as a set of raw observations. The differing coloration of the dots is primarily to allow for articulate viewing (i.e., so the reader is not presented with a large wash of undifferentiated uniform color) and also to provide the opportunity to observe any time dependence in the distribution of the values. We do not claim to detect a noticeable time-dependent trend in the case of this figure; however, in Fig. 9, there does appear to be some noticeable time-dependence.

In Fig. 9, we investigate the relationship between (squared) eccentricity and ring count. As with area versus ring count, it is not obvious what the relationship between eccentricity and ring count should be: If eccentricity was determined purely by the shape of each note, then we would expect a "quantized" set of eccentricities (one for each note-shape), but instead, we see a wide range of antinode eccentricities present. (The horizontal banding near the bottom is a non-physical artifact of pixel-integer math.) In the case of this figure, we observe that the darker dots representing early times tend to cluster in the upper right area of high eccentricity and low ring count, whereas the domain of low eccentricity and high ring count tends to be occupied only at later times. We will discuss this further in Sec. V.

A sample movie of SPNet-annotated video frames is available in the Supplementary Materials, as well as at <https://youtu.be/-rJLwcbQ7Kk>.

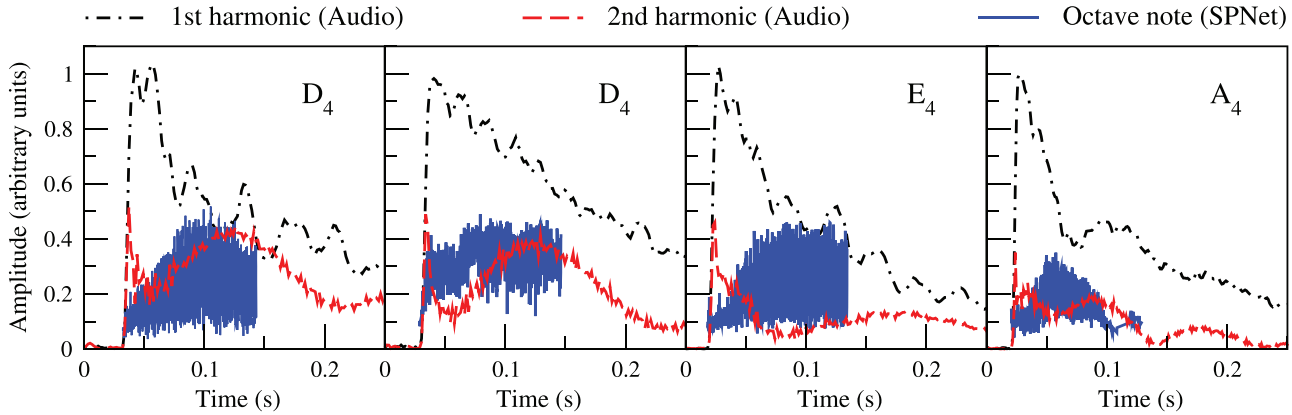


FIG. 7. (Color online) Time series for four (manual) drum strikes on fundamental notes D_4 , D_4 again, E_4 and A_4 . The solid (blue) line shows the rapid oscillation in ring counts from SPNet’s annotations of the corresponding octave note, for which absolute-value cosine curve fits show frequencies at or very close to the expected 2nd harmonic frequencies (i.e., D_5 , E_5 and A_5 , respectively). Dot-dashed (black) and dashed (red) lines show the amplitude obtained from audio recordings of the events, for the 1st and 2nd harmonics, respectively. The richness of the drum’s behavior is evident from the variability between strikes. All graphs show a rapid damping of the 2nd harmonic immediately after the initial strike, yet the later rise in the 2nd harmonic sound intensity significantly lags (or is even uncorrelated with) the motion of the corresponding octave note observed in video analysis by SPNet. Even in the left-most graph where the two appear to correspond, the lag is significantly longer than would be suggested by physical delay mechanisms such as wave travel time. We discuss these further in Sec. V. (The SPNet annotations end before the audio recordings because high-speed video was only recorded for ≈ 150 ms.)

V. DISCUSSION

A. Physical Interpretation

In Fig. 7 we observe the differing behavior of the second harmonics when measured via audio versus SPNet (via the latter’s ring-count annotations of the octave note). We find this difference surprising, as we would expect these two signals to exhibit close similarity.

In Fig. 7(a), the audio signals for the first and second harmonics initially decay at approximately the same rate (i.e., they have the same “reverberation time”), suggesting that this initial transient in the second harmonic sound results from the first harmonic note ringing down as a

superposition of first and second harmonics, and only later does the octave note in the drum begin to oscillate significantly—on differing time scales of roughly 50 ms after the strike for in the video (SPNet output) and 150 ms for the audio. The strike shown in Fig. 7(b) exhibits qualitatively different behavior from the previous graph. The second harmonic in the audio initially decays much faster than the fundamental, and rises again 90 ms later, whereas the octave note as measured by SPNet begins oscillating immediately and maintains its amplitude.

The drum strikes were performed by hand, not always with the same velocity or even exactly in the same location within each fundamental note, so that differences between

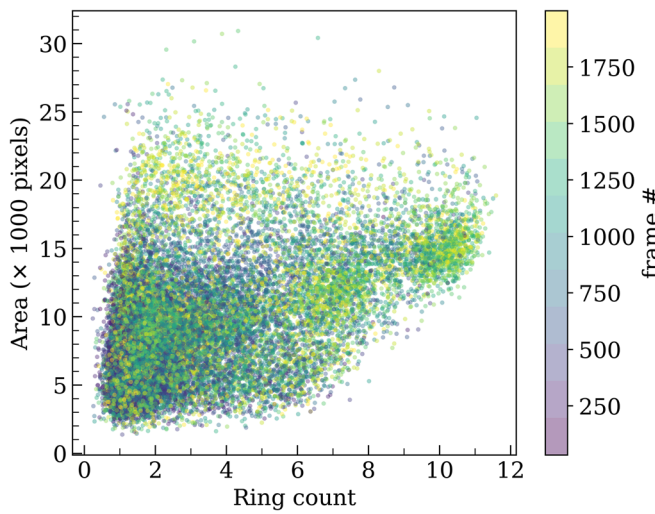


FIG. 8. (Color online) Area versus number of rings for antinodes detected in four separate videos of drum strikes. The largest ring-counts are associated with large areas, however as expected, the reverse is not the case, for physical reasons described in the text. We color the points by the frame number in each video, as a way to investigate how the distribution of area versus ring count might change over time (although we make no claims for this figure).

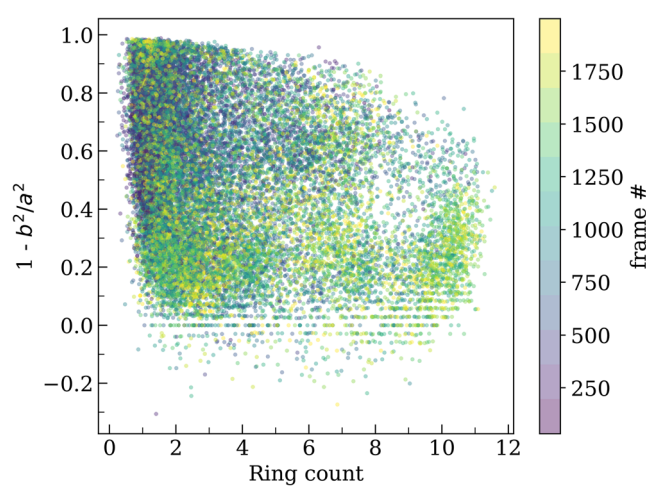


FIG. 9. (Color online) Eccentricity squared versus ring count. We observe that dark-colored dots representing antinodes at early times tend to cluster towards the upper left area of higher eccentricity and low ring count, whereas lower eccentricities with larger ring counts are seen mostly at later times (lighter colors). For nearly circular antinodes, the model is not prevented from predicting $b > a$ sometimes (by as much as 7 pixels), despite being trained on data for which $a > b$ is always satisfied; hence the negative values of $1 - b^2/a^2$.

Figs. 7(a) and 7(b) need not merit consternation in their own right. One may add to this the fact that these two different drum notes were hand-hammered by the steelpan tuner and thus, there is no guarantee of consistency from one note to the next.

Allowing for such variations, however, the difference (for each strike) in the second harmonic between audio and video (SPNet annotation) measurements is nevertheless noteworthy. At present, we are unable to account for this discrepancy. Looking at the graphs of the signals (physics aside), one might propose some kind of “delay” of at least 50 ms between the two signals, at which point it is worth ruling out two mechanisms that would not produce such a long-term effect. First, the travel time of sound in air from the drum to the microphone is no more than 3 ms since the latter is only 1 m away. Second, the wave speed in the drum is roughly 3000 m/s (this is not a precise number because steelpans, like the one used in this study, are hand-hammered by artisans and thus contain variations in thickness), whereas the distance between the fundamental and octave notes is at most a few centimeters, yielding a wave travel time in the drum on the order of $10 \mu\text{s}$. Given that the dynamical time scales for wave travel are so short, it seems unlikely that the difference in signals can be accounted for in terms of a delay due to wave propagation. Thus, an understanding of the physics producing the observed difference in the measurements for the second harmonic awaits further study.

Turning our attention to the distribution of eccentricity versus ring count as shown in Fig. 9, we observe an apparent trend of clustering of early-time antinodes towards the upper left, with the lower right consisting of mostly later-time antinodes. This raises several questions, as the interpretation of this observation is not straightforward. While this trend is truly present in the data (and not some artifact of the order in which points are plotted), we prefer caution about drawing physical inferences from this. The idea that large, circular antinodes are the ones likely to persist the longest seems well-motivated, but the evolution of a single antinode is not trackable in this figure: We saw in the second harmonic graphs of Fig. 7, ring counts not only decrease with time via damping but can increase over time. (Also, since the frames show oscillating antinodes, each dot in the graph oscillates left-and-right “rapidly” in this figure, regardless of any longer-term trends). Apart from the “path” through this graph-space that an individual antinode might take over time, it is unclear whether “missing” data points have any physical significance. For example, in this data there is an absence at early times of low-eccentricity antinodes with high ring counts, and yet we know that the note at which the drum is struck oscillates with an essentially circular shape, with high ring count. Is it then the case that the “missing” circular, high-ring-count antinodes do not occur, or is it merely that these are not detected (i.e., false negatives) by the model? The latter scenario seems likely, given that many volunteers in the SVP failed to annotate the large initial strike area. One might similarly conjecture whether the

“hole” seen around the coordinates (9, 0.4) is physically interesting, or is a mere artifact of the available notes on the drum (i.e., the finite number of notes, and/or the choice of the experimenters on which notes they recorded), or an artifact of the object detector. These questions bear further investigation.

B. Machine Learning Considerations

Rather than producing a generic object detector package for measuring interference fringes in all forms of musical instruments illuminated by ESPI, we have trained a model to assist in filling in missing annotations (“in-between frames”) for a small set of videos focused on a particular region of a particular steelpan drum. While the methods used in this paper could be replicated in other domains if sufficient training data (i.e., annotated video frames) were available, the question of how well our model, trained on such images as we have, could predict interference fringes in more general situations, remains open. One would hope that transfer learning⁵⁷ could be applied using our model as a starting point for similar ESPI images, lowering the requirement for new training data. Earlier we stated that using transfer learning using ImageNet weights proved no better than starting from scratch, but the similarity between ESPI images (versus their difference from typical ImageNet images) could prove beneficial.

Not all instruments exhibit elliptical-shaped antinode regions; however, we conjecture that the shape is not a primary limiting factor if one wishes to count fringes apart from requiring precise bounds on the antinode regions. Some early work we performed using image-segmentation model Mask-RCNN^{58,59} indicated it could find peanut-shaped and triangle-shaped antinode regions, even when trained on ellipses; however, the code structured on a deep level as a classifier and we elected not to try to modify it for regression.

The variability in the human annotations of the real data prevented us from objectively scoring highly when evaluating the model (because even the testing set exhibited the same inconsistencies), and although using the fake data (particularly CGSmall) allowed us to gauge how well the model might perform on consistently annotated ESPI images, these fake data were not physically motivated. An alternate path to obtaining physically realistic training data would be to perform physical simulations of the steelpan⁶⁰ via methods such as Finite Element modeling^{61,62} and then apply “styling” techniques, such as CycleGAN, to make the fake images look like the real ones.

VI. CONCLUSIONS

Using an object detector comprised of convolutional neural networks, it is possible to locate and track antinode regions on oscillating steelpan drums, and to solve the regression task of estimating the number of interference rings in each antinode. While variations in the human annotations prevented high scores on accuracy metrics, our

“SPNet” model’s performance was sufficient to extract oscillation information at the correct frequencies in highly time-dependent, transient regimes. Data from our analysis indicate a significant discrepancy between audio recordings of second harmonic oscillations (sympathetic to a drum struck on a fundamental note) and optical measurements (i.e., video frame analysis by SPNet). Explaining this discrepancy in terms of likely physical processes remains beyond the scope of our current effort. Subsequent analysis published in future papers may reveal additional insights.

ACKNOWLEDGMENTS

The authors thank Thomas R. Moore for helpful consultation during the completion of this paper and Matthew Lange who assisted A.C. M. with data processing and was supported by NSF Grant No. 1741934. This publication uses data generated via the Zooniverse.org platform, development of which is funded by generous support, including a Global Impact Award from Google, and by a Grant from the Alfred P. Sloan Foundation.

¹T. Moore, “Measurement techniques,” in *Springer Handbook of Systematic Musicology* (Springer Berlin Heidelberg, 2018), pp. 81–103.

²E. Bakarezos, Y. Orphanos, E. Kaselouris, V. Dimitriou, M. Tatarakis, and N. A. Papadogiannis, “Laser-based interferometric techniques for the study of musical instruments,” in *Current Research in Systematic Musicology* (Springer International Publishing, 2019), pp. 251–268.

³B. Richardson, “Mode studies of plucked stringed instruments: Application of holographic interferometry,” *J. Acoust. Soc. Am.* **129**, 2615–2615 (2011).

⁴T. R. Moore, A. E. Cannaday, and S. A. Zietlow, “A simple and inexpensive optical technique to help students visualize mode shapes,” *J. Acoust. Soc. Am.* **131**(3), 2480–2487 (2012).

⁵A. C. Morrison, T. R. Moore, and D. Zietlow, “High speed electronic speckle pattern interferometry as a method for studying the strike on a steelpan,” *J. Acoust. Soc. Am.* **129**(4), 2615–2615 (2011).

⁶W. R. Aho, “Steel band music in Trinidad and Tobago: The creation of a people’s music,” *Lat. Am. Music Rev. / Rev. Música Latinoam.* **8**(1), 26–58 (1987).

⁷A. C. Morrison, T. Moore, and D. Zietlow, “Searching for early reflected waves after strike of Caribbean steelpan using time-resolved electronic speckle pattern interferometry,” *J. Acoust. Soc. Am.* **142**(4), 2544 (2017).

⁸S. E. Maloney, “Acoustics and manufacture of Caribbean steelpans,” Ph.D. dissertation (Wolfson College, Oxford, UK, 2010).

⁹M. Monteil, C. Touzé, and O. Thomas, “Nonlinear vibrations of steelpans: Analysis of mode coupling in view of modal sound synthesis,” in *SMAC Stockholm Music Acoustics Conference 2013*, Stockholm, Sweden, (July 30–August 3, 2013), p. 7.

¹⁰A. C. Morrison, “Steelpan Vibrations,” <https://www.zooniverse.org/projects/achmorrison/steelpan-vibrations> (2017) (Last viewed August 25, 2021).

¹¹K. D. Borne and Z. Team, “The Zooniverse: A framework for knowledge discovery from citizen science data,” in *AGU Fall Meeting Abstracts*, San Francisco, CA, (December 5–9, 2011).

¹²K. W. Willett, M. A. Galloway, S. P. Bamford, C. J. Lintott, K. L. Masters, C. Scarlata, B. D. Simmons, M. Beck, C. N. Cardamone, E. Cheung, E. M. Edmondson, L. F. Fortson, R. L. Griffith, B. Häußler, A. Han, R. Hart, T. Melvin, M. Parrish, K. Schwinski, R. J. Smethurst, and A. M. Smith, “Galaxy Zoo: Morphological classifications for 120000 galaxies in HST legacy imaging,” *Mon. Not. R. Astron. Soc.* **464**(4), 4176–4203 (2017).

¹³J. A. Garcia and A. Morrison, “Evaluating the use of crowdsourced data classifications in an investigation of the steelpan drum,” in *Proceedings of Meetings on Acoustics 174ASA*, New Orleans, LA, ASA (December 4–8, 2017), Vol. 31, p. 035001.

¹⁴H. K. Yuen, J. Illingworth, and J. Kittler, “Ellipse detection using the Hough Transform,” in *Proceedings of the Alvey Vision Conference*, University of Manchester, Manchester, UK (1988), pp. 41.1–41.8.

¹⁵W. Lu and J. Tan, “Detection of incomplete ellipse in images with strong noise by iterative randomized hough transform (IRHT),” *Pattern Recognit.* **41**(4), 1268–1279 (2008).

¹⁶Z.-Y. Liu and H. Qiao, “Multiple ellipses detection in noisy environments: A hierarchical approach,” *Pattern Recognit.* **42**(11), 2421–2433 (2009).

¹⁷Y. LeCun, C. Cortes, and C. J. Burges, “MNIST handwritten digit database,” ATT Labs 2, (2010) [Online]. Available: <http://yann.lecun.com/exdb/mnist>. (Last viewed August 25, 2021).

¹⁸A. Krizhevsky, I. Sutskever, and G. E. Hinton, “Imagenet classification with deep convolutional neural networks,” *Adv. Neural Inf. Process. Syst.* **1**, 1097–1105 (2012).

¹⁹K. He, X. Zhang, S. Ren, and J. Sun, “Deep residual learning for image recognition,” in *Proceedings of the IEEE Conference on Computer Vision and Pattern Recognition*, Las Vegas, NV, (June 26–July 1, 2016), pp. 770–778.

²⁰P. Viola and M. Jones, “Rapid object detection using a boosted cascade of simple features,” in *Computer Vision and Pattern Recognition, 2001. CVPR 2001. Proceedings of the 2001 IEEE Computer Society Conference On*, IEEE (2001), Vol. 1, pp. I–I.

²¹A. Douillard, “Object detection with deep learning on aerial imagery,” Medium.com (2018), <https://medium.com/data-from-the-trenches/object-detection-with-deep-learning-on-aerial-imagery-2465078db8a> (Last accessed January 27, 2021).

²²C. Zheng, J. Pulido, P. Thorman, and B. Hamann, “An improved method for object detection in astronomical images,” *Mon. Not. R. Astron. Soc.* **451**(4), 4445–4459 (2015).

²³R. E. González, R. P. Muñoz, and C. A. Hernández, “Galaxy detection and identification using deep learning and data augmentation,” *Astron. Comput.* **25**, 103–109 (2018).

²⁴J. Redmon, S. Divvala, R. Girshick, and A. Farhadi, “You only look once: Unified, real-time object detection,” in *Proceedings of the IEEE Conference on Computer Vision and Pattern Recognition*, Las Vegas, NV, (June 26–July 1, 2016), pp. 779–788.

²⁵R. Girshick, J. Donahue, T. Darrell, and J. Malik, “Rich feature hierarchies for accurate object detection and semantic segmentation,” in *Proceedings of the IEEE Conference on Computer Vision and Pattern Recognition*, Columbus, OH, (January 24–27, 2014), pp. 580–587.

²⁶W. Liu, D. Anguelov, D. Erhan, C. Szegedy, S. Reed, C.-Y. Fu, and A. C. Berg, “Ssd: Single shot multibox detector,” in *European Conference on Computer Vision* (Springer, 2016), pp. 21–37.

²⁷J. Redmon and A. Farhadi, “YOLO9000: Better, faster, stronger,” in *2017 IEEE Conference on Computer Vision and Pattern Recognition (CVPR)*, IEEE (Honolulu, HI, 2017), pp. 6517–6525.

²⁸J. Deng, W. Dong, R. Socher, L.-J. Li, K. Li, and L. Fei-Fei, “Imagenet: A large-scale hierarchical image database,” in *2009 IEEE Conference on Computer Vision and Pattern Recognition*, IEEE (2009), pp. 248–255.

²⁹F. H. C. Tivive and A. Bouzerdoum, “Texture classification using convolutional neural networks,” in *TENCON 2006 - 2006 IEEE Region 10 Conference* (2006), pp. 1–4.

³⁰R. Geirhos, P. Rubisch, C. Michaelis, M. Bethge, F. A. Wichmann, and W. Brendel, “Imagenet-trained CNNs are biased towards texture; increasing shape bias improves accuracy and robustness,” in *International Conference on Learning Representations* (2019). <https://openreview.net/forum?id=Bygh9j09KX>

³¹Z. Zou, Y. Cheng, X. Qu, S. Ji, X. Guo, and P. Zhou, “Attend to count: Crowd counting with adaptive capacity multi-scale cnns,” *CoRR abs/1908.02797* (2019). <http://arxiv.org/abs/1908.02797>. (Last accessed January 27, 2021).

³²S. Pan, S. Fan, S. W. K. Wong, J. V. Zidek, and H. Rhodin, “Ellipse detection and localization with applications to knots in sawn lumber images,” *arXiv:2011.04844cs.CV* (2020).

³³S. H. Hawley, “SPNet Dataset Release,” (2021), <https://doi.org/10.5281/zenodo.4445434>.

³⁴F. Chollet, “Xception: Deep learning with depthwise separable convolutions,” in *2017 IEEE Conference on Computer Vision and Pattern Recognition (CVPR)* (2017), pp. 1800–1807.

³⁵A. G. Howard, M. Zhu, B. Chen, D. Kalenichenko, W. Wang, T. Weyand, M. Andreetto, and H. Adam, “Mobilenets: Efficient convolutional neural

networks for mobile vision applications," arXiv preprint [arXiv:1704.04861](https://arxiv.org/abs/1704.04861) (2017).

³⁶C. Szegedy, S. Ioffe, and V. Vanhoucke, "Inception-v4, Inception-ResNet and the impact of residual connections on learning," CoRR abs/1602.07261 (2016). <https://arxiv.org/abs/1602.07261>.

³⁷F. Chollet *et al.*, "Keras," (2015). <https://github.com/fchollet/keras>.

³⁸J. Deng, W. Dong, R. Socher, L.-J. Li, K. Li, and L. Fei-Fei, "ImageNet: A large-scale hierarchical image database," in *CVPR09* (2009).

³⁹H. Li, Z. Xu, G. Taylor, C. Studer, and T. Goldstein, "Visualizing the loss landscape of neural nets," in *Advances in Neural Information Processing Systems*, edited by S. Bengio, H. Wallach, H. Larochelle, K. Grauman, N. Cesa-Bianchi, and R. Garnett (Curran Associates, Inc., 2018). Vol. 31, pp. 6389–6399.

⁴⁰N. Srivastava, G. Hinton, A. Krizhevsky, I. Sutskever, and R. Salakhutdinov, "Dropout: A simple way to prevent neural networks from overfitting," *J. Mach. Learn. Res.* **15**(56), 1929–1958 (2014); <https://openreview.net/forum?id=B1lz-3Rct7> (Last accessed September 20, 2021).

⁴¹A. Saxena, J. Driemeyer, and A. Y. Ng, "Learning 3-D object orientation from images," in *2009 IEEE International Conference on Robotics and Automation* (2009), pp. 794–800.

⁴²J.-Y. Zhu, T. Park, P. Isola, and A. A. Efros, "Unpaired image-to-image translation using cycle-consistent adversarial networks," in *Computer Vision (ICCV), 2017 IEEE International Conference on* (2017).

⁴³The reason for avoiding rotations and translations while training is that these might cause ellipses to jump discontinuously from one assigned predictor to another; the code could be made to handle that but it currently does not.

⁴⁴T. DeVries and G. W. Taylor, "Improved regularization of convolutional neural networks with Cutout," [arXiv:1708.04552](https://arxiv.org/abs/1708.04552) [cs] (2017).

⁴⁵A. Krogh and J. A. Hertz, "A simple weight decay can improve generalization," in *Proceedings of the 4th International Conference on Neural Information Processing Systems*, Denver, CO, NIPS'91 (December 2–5, 1991), pp. 950–957.

⁴⁶G. Zhang, C. Wang, B. Xu, and R. Grosse, "Three mechanisms of weight decay regularization," in *International Conference on Learning Representations*, New Orleans, LA, (Last viewed May 6–9, 2019). <https://openreview.net/forum?id=B1lz-3Rct7> (Last viewed).

⁴⁷F. Chollet *et al.*, "Layer weight regularizers," (2021). <https://keras.io/api/layers/regularizers/> (Last viewed January 30, 2021).

⁴⁸L. N. Smith, "A disciplined approach to neural network hyper-parameters: Part 1 - Learning rate, batch size, momentum, and weight decay," CoRR abs/1803.09820 (2018). [http://arxiv.org/abs/1803.09820](https://arxiv.org/abs/1803.09820).

⁴⁹S. Gugger and J. P. Howard, "Callbacks.one_cycle, Fastai," (2019), https://docs.fast.ai/callbacks.one_cycle.html (Last accessed May 25, 2019).

⁵⁰I. Loshchilov and F. Hutter, "SGDR: Stochastic gradient descent with restarts," CoRR [abs/1608.03983](https://arxiv.org/abs/1608.03983) (2016). <http://arxiv.org/abs/1608.03983>.

⁵¹Even though ours is a regression problem, the accuracy metric emulates a classification metric, as object detectors are typically classifiers. Our metric of "within ± 0.5 " makes more sense than rounding predicted and ground truth ring counts each to the nearest integer, so that for example, by our metric, a prediction of 5.4 rings compared to a ground truth of 5.6 is counted as a "correct" (or "matching") classification rather than an incorrect one.

⁵²S. Bailey, "Step-by-step explanation of scoring metric," in *2018 Data Science Bowl*, Kaggle.com (2018), <https://kaggle.com/stkbailey/step-by-step-explanation-of-scoring-metric> (Last viewed January 21, 2021).

⁵³T.-Y. Lin, M. Maire, S. Belongie, L. Bourdev, R. Girshick, J. Hays, P. Perona, D. Ramanan, C. L. Zitnick, and P. Dollár, "Microsoft coco: Common objects in context," (2015).

⁵⁴L. Vazquez and F. Hassainia, "Icevision: An agnostic computer vision framework," (2020). <https://github.com/airetic/IceVision>.

⁵⁵A Google Colab notebook for the baseline IceVision-based mAP calculation is available at <https://tinyurl.com/spnelt-icevision> (Last viewed August 25, 2021).

⁵⁶A. Morrison, D. Zietlow, and T. Moore, "Time-resolved interferometry and phase vocoder analysis of a caribbean steelpan," in *SMAC Stockholm Music Acoustics Conference 2013* (Stockholm, Sweden, 2013), pp. 563–568.

⁵⁷K. Wang, X. Gao, Y. Zhao, X. Li, D. Dou, and C.-Z. Xu, "Pay attention to features, transfer learn faster CNNs," in *International Conference on Learning Representations*, Addis Ababa, Ethiopia (April 26–May 1, 2020). <https://openreview.net/forum?id=ryxyCeHbP>.

⁵⁸K. He, G. Gkioxari, P. Dollar, and R. Girshick, "Mask R-CNN," in *Proceedings of the IEEE International Conference on Computer Vision (ICCV)*, Venice, Italy (1991) (October 22–29, 2017).

⁵⁹W. Abdulla, "Mask R-CNN for object detection and instance segmentation on keras and tensorflow," https://github.com/matterport/Mask_RCNN (2017) (Last viewed January 21, 2021).

⁶⁰Y. Kagawa, K. Tanaka, K. Yamazaki, and L. Chai, "Modeling and simulation of the acoustics of a steelpan, a percussion instrument," in *Advanced Methods, Techniques, and Applications in Modeling and Simulation* (Springer, Japan, 2012), pp. 32–40.

⁶¹D. A. Gay, "Finite element modelling of steelpan acoustics," *J. Acoust. Soc. Am.* **123**(5), 3799–3799 (2008).

⁶²M. Monteil, O. Thomas, J. Frelat, C. Touzé, and W. Seiler, "Towards a steelpan making model - Residual stress field effects on dynamical properties," in *Acoustics 2012*, edited by S. F. d'Acoustique (Acoustics, Nantes, France, 2012).